4168 *J. Phys. Chem. A* **2009,** *113,* 4168–4174

Deformation and Hyperfine Structures of Dendrimers Investigated by Scanning Tunneling Microscopy[†]

Christopher J. Fleming, Ying X. Liu, Zhao Deng, and Gang-yu Liu*

Department of Chemistry, University of California, Davis, California 95616

Received: December 1, 2008; Revised Manuscript Received: January 22, 2009

Scanning tunneling microscopy (STM) is known to provide the highest spatial resolution in real space imaging of materials, and its applications are most common among conductive and semiconductive systems. The high tunneling barrier of insulators diminishes the tunneling probability and thus compromises STM's resolution. This work introduces a simple method to approach this problem, by using STM for high-resolution imaging of insulating materials such as the fourth and fifth generations of poly(amidoamine) hydroxyl-terminated dendrimers. The tunneling barrier is lowered by precoordination with Cu(II) or Pt(II) ions, enabling intramolecular hyperfine features be resolved with 0.2 nm resolution. The spatial distribution, size, and overall number of hyperfine features are consistent with the location of dendrimer termini. The immobilization process deforms dendrimers from the spherical geometry in solution phase to asymmetrical domes in ambient. The ultrahigh vacuum (UHV) environment leads to a higher degree of deformation with reduction of volume. The high-resolution images enable the determination of fundamental parameters of individual dendrimers, including axis, height, asymmetry, and volume. From STM spectroscopy and prior knowledge of dendritic systems, the STM imaging mechanism under UHV is consistent with metal(0) nanoparticles encapsulated by dendrimers, while ambient imaging is most likely via metal-ion-facilitated charge transport. The results from this investigation bring us one step closer toward structural characterization at atomistic level and should enable direct comparison of dendrimer structures with simulations, and deepen our understanding of charge transport in dendrimer systems.

Introduction

Surface-bound dendrimers have attracted much interest due to promising applications in molecular electronics, sensing devices, and heterogeneous catalysis.[1−4] In addition, immobilization enables high-resolution structural characterization such as using transmission electron microscopy,[3,5] neutron and X-ray diffraction,[6] as well as scanning probe microscopy.[7,8] Atomic level characterization is of fundamental importance in facilitating the design of dendrimer molecules and dendrimer-based devices, in dendrimer-based drug delivery, where specific termini or intramolecular moieties are utilized to carry drugs,[4,9] as well as in deepening our understanding of intramolecular and dendrimer−surface interactions for this fascinating class of molecules.

In the past decade, much effort was devoted to attaining high-resolution structural characterization of dendrimers. Atomic force microscopy (AFM) was utilized to reveal the deformation of dendrimers upon immobilization on surfaces.[7,10−14] The heights of fourth generation (G4) and eighth generation (G8) poly(amido-amine), i.e., G4- and G8-PAMAM-NH_3 dendrimers, have been determined while inlaid in alkanethiol self-assembled monolayers (SAMs).[12] The thiol SAMs hold dendrimers in place by laterally compressing dendritic molecules to enhance the integrity.[12] The deformation of dendrimers on mica surfaces of 5th through 10th generation PAMAM dendrimers has been investigated using AFM, finding that higher generation dendrimers deform less due to a rigidity caused by close packing of the outer branches.[6,13,14] Additional AFM studies showed that the packing and deformation depend on intramolecular forces and dendrimer−surface interactions and may be changed externally, e.g., by variations of dendrimer concentration or pH.[7,11,15] While AFM is a powerful tool in visualizing dendrimer packing and deformation, as well as in height determination, resolving intramolecular features is very difficult due to the issue of tip convolution[16] and nonatomic nature of tip−dendrimer contact under imaging.[17]

Scanning tunneling microscopy (STM), due to its capability in resolving subatomic features,[18−20] was also used to characterize the structure of dendrimers.[21,22] The difficulty arises from the nonconductive nature of most dendrimers, especially in high generations. These systems presented high-energy barriers and, thus, little tunneling probability. Efforts to lower the barriers included incorporation of more conductive functionalities such as metallic porphyrins,[23] and phenyl rings[24] as well as implementation of metal nanoparticles by a two-step reaction of coordination and reduction.[1,22] These approaches led to important advances. The STM images of heptanuclear Ru(II) dendrimers showed three domains due to the conformational arrangement of each dendrimer repeating unit.[25] Multiple Zn(II) porphyrin units in dendrimers enabled intramolecular features such as a petal-like shape or concentrical necklace arrangement be revealed at the cryo temperatures of liquid nitrogen.[24] In the study of single electron tunneling (SET) at room temperature, a certain degree of intramolecular contrast was observed by placing a metal nanoparticle (NP) within a dendrimer.[26] These advances were very encouraging in continuing the use of STM for structural characterization toward atomic level.

The goal of this work is to develop a simple and more generic approach toward atomic level imaging of insulating materials

---

[†] Part of the "George C. Schatz Festschrift".

* Author to whom correspondence should be addressed. Phone: 530-754-9678. Fax: 530-754-8557. E-mail: liu@chem.ucdavis.edu.

10.1021/jp810535g CCC: $40.75

such as dendrimers using STM. Using PAMAM-OH dendrimers to initiate the investigation, we saturate the intramolecular tertiary amine moieties with Pt(II) or Cu(II) ions before depositing them on surfaces. The coordination of metal ions significantly enhances the electron transport efficiency, thus enabling visualization of intramolecular features such as termini at room temperature. The possible STM imaging mechanism will also be discussed.

Experimental Methods

Materials. Fourth generation PAMAM-OH dendrimer solutions (10% weight in methanol, Sigma-Aldrich), fifth generation PAMAM-OH dendrimer solutions (5% weight in methanol, Sigma-Aldrich), *n*-octanethiol (98%, Sigma-Aldrich), and *n*-decanethiol (96%, Sigma-Aldrich), referred to hereafter as C_8 and C_{10}. $Cu(CH_3COO)_2$ (99.999%, Sigma-Aldrich) were obtained and used without further purification. Na_2PtCl_4 and K_2PtCl_4 (min. 42.4% Pt, Alfa Aesar) was used as received. Ultrapure water ($\geqslant$18 MΩ, Millipore Milli-Q) and 200 proof ethanol (Gold Shield Chemical Co.) were used for sample dilution and washing. Ultrapure N_2 ($\geqslant$98%, Air Gas Co.) and H_2 (99.99%, Praxair, Inc.) were used as obtained. STM tips were made from W wire (d = 0.010 in., 99.95%, California Fine Wire Co.). For substrate preparation, Au (99.99%, Alpha Aesar Premion Co.) was used, in conjunction with clear ruby muscovite mica (Mica New York Corp.).

Substrate Preparation. Au(111) substrates were prepared through vapor deposition of Au onto freshly cleaved mica in a high-vacuum evaporator (Denton Vacuum, model 502-A).[27] The substrate mica was maintained via two quartz lamps at 350 °C under a base pressure of 2×10^{-7} Torr. The evaporation rate was 0.3 nm/s and final thickness of Au films were 170−190 nm. After evaporation, the gold was thermally annealed in situ at 375 °C for 30−60 min.

Immobilization of Metal-Ion-Coordinated Dendrimers on Surfaces. Dendrimer solutions were prepared following previously established procedures.[1] In short, PAMAM-OH-$(M^{2+})_n$ dendrimer solutions were made by diluting aliquots of the methanol-based stock solutions using ultrapure H_2O to 1.25 μM. Pt(II) or Cu(II) compounds were dissolved in MilliQ water to 350 μM. The mixing of dendrimer (4.0 mL) and metal(II) (1.0 mL) was carried out according to designed molar ratios such as: 1:20 or 1:70 dendrimer:metal(II). Once mixed, the solution was kept in room temperature for 3−5 days, allowing sufficient time for metal ion−amine coordination within dendrimers.[28] UV−vis spectroscopy (model DU 640i spectrophotometer, Beckman Instruments, Inc.) was employed to monitor metal ion uptake and determine the reaction equilibria.[3,29] The dendrimer−Pt(II) coordination was monitored via absorbance at λ = 220 and 250 nm, and the maximum absorbance intensity was reached at 48 h. Dendrimer−Cu(II) coordination was monitored via absorbance at λ = 615 nm, and the equilibrium was reached at 45 h.[29] To ensure metal coordination, a minimum of 2.5 days mixing time was allowed for each sample before deposition on surfaces for STM imaging.

For depositing dendrimers on surfaces, 1 cm^2 pieces of gold films were H_2-flamed,[27] and allowed to cool for 10 min under clean ambient conditions. Then a 50−150 μL drop of PAMAM-OH-$(M^{2+})_n$ solution was deposited to the Au surface and allowed to remain for 35−120 s to reach desired surface coverage. The sample was then washed with Milli-Q water and ethanol and finally exposed to 1.0−1.5 mM C_8 solution for 1.5−12 min to obtain high dendrimer surface coverage or 10−12 min for low dendrimer surface coverage. The sample was then washed again with ethanol and allowed to dry in a clean container for 0.75−1.5 h, before STM imaging.

Ambient STM Imaging and Spectroscopy. The scanning tunneling microscope has an UHV 300 scanner from RHK Technologies, Inc., and was used in ambient conditions. The STM tips used for these studies were W wires electrochemically etched in 3.0 M NaOH solutions. A homemade potentiostat monitored and controlled the etching process.[27,30] All STM images were acquired in constant current mode with typical bias voltages ranging from 0.3 to 1.1 V and tunneling currents from 5 to 40 pA. Tips were typically etched using 2.0 V and in a 3.0 M NaOH solution. The STM piezoelectric scanners were calibrated laterally (4.99 Å NN lattice constant) and vertically (2.35 Å step height) using a decanethiol SAM on Au(111). Calculation of dendrimer−surface contact area was accomplished using the ImageJ program (National Institutes of Health, Bethesda, MD). Single dendrimer $I-V$ measurements were acquired according to the following systematic steps.[30] First, the surface was scanned and individual dendrimer molecules were visualized. Second, the scan area was reduced to include the selected dendrimer, e.g., to a 10×10 nm^2 area. Finally, the STM tip was positioned over the center of the dendrimer molecule for acquiring $I-V$ spectra.

UHV STM Imaging and Spectroscopy. The UHV STM has a walker type scanner (UHV 300, model number 514, RHK Technologies, Inc.)[27,30−33] and was operating at a base pressure of 2×10^{-10} Torr. The UHV system has a rapid-entry load lock for sample and tip exchange and is equipped with a mass spectrometer (Prisma QMS 200, Balzers, Ltd.) and an Ar ion sputtering gun (AG 5000, Fisons Instruments, Inc.). All STM images were taken within the set point ranges of 0.3−1.1 V and 5−40 pA. The STM tip preparation, scanner calibration, imaging, and spectroscopy followed similar protocols as that of ambient studies.

AFM Imaging and Determination of Dendrimer Height. AFM images were acquired using a MFP3D-SA system (Asylum Research, Santa Barbara, CA), which includes closed loop capabilities with special precision of 0.6 nm × 0.6 nm × 0.3 nm. A silicon cantilever (AC-240, Olympus, Japan) was used for imaging and nanoshaving,[34] with a force constant of k = 1.0 N/m, measured by a thermal noise method.[35] During AFM tapping mode imaging, the cantilever is modulated by a driving frequency of 68 kHz and amplitude of 0.13 V, the damping is set to 85−90%. For displacing adsorbates (such as dendrimers and thiols), tips were placed in contact with the surface with increasing deformation or load until complete displacement. Cursor profiles were taken on AFM topographs prior to any image processing.

Results and Discussion

Morphology of Surface Immobilized Dendrimers. High-resolution ambient STM imaging reveals deformation of dendrimers on surfaces from their spherical shape in solution phase. Figure 1A is an STM topograph showing a high coverage of G4-PAMAM-OH-$(Pt^{2+})_{70}$ on Au(111). The highest protrusions in Figure 1A correspond to individual dendrimers immobilized on the Au(111) surface. Figure 1B is a high-resolution view (13×13 nm^2) of the same surface, for which the geometry and separation of dendrimers are clearly visualized. The long (a) and short (b) axes of the selected dendrimer are extracted from cursor profiles 1 and 2 and measure 6.0 and 5.3 nm, respectively; i.e., the immobilized dendrimers assume an elliptical dome shape. The STM apparent height (h_{APP}), defined as the top of the dendrimer to the lowest point in the SAM

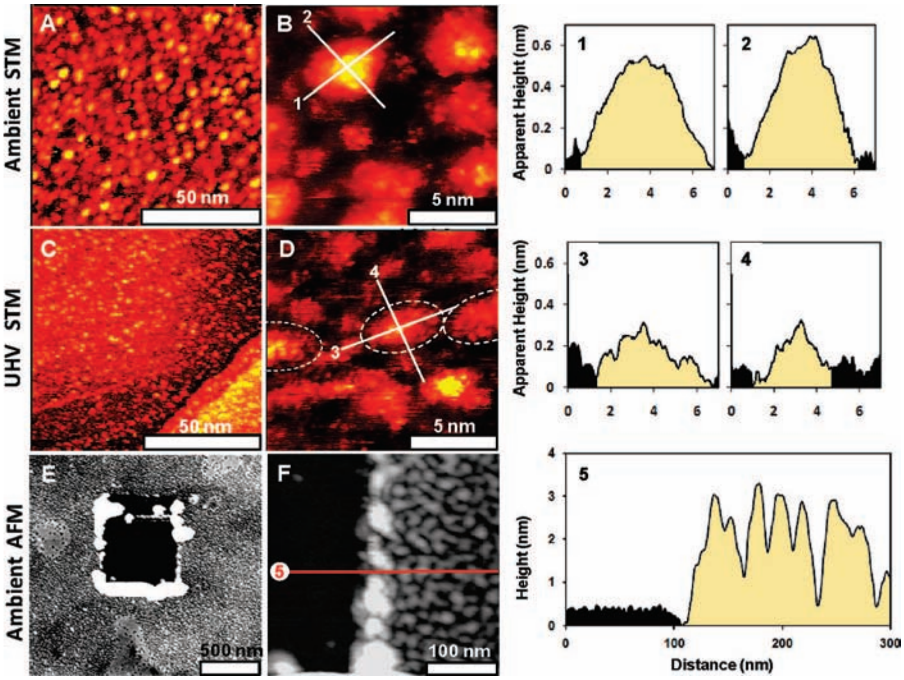

Figure 1. STM and AFM images of G4-PAMAM-OH-Pt dendrimers on Au(111) prepared under identical conditions. (A) A 100 × 100 nm^2 STM topograph acquired under ambient conditions. (B) A 13 × 13 nm^2 zoom in view of the same sample. (1) A cursor plot from (B) corresponding to ambient measurement of *a*, and (2) a cursor plot from (B) corresponding to the measurement of *b*. (C) A 100 × 100 nm^2 STM topograph acquired under UHV conditions. (D) A 13 × 13 nm^2 zoom-in view of the same sample. (3) A cursor plot from (D) corresponding to UHV measurement of *a*, and (4) a cursor plot from D corresponding to UHV measurement of *b*. (E) A 1.8 × 1.8 μm^2 AFM image on the same sample as in (A) and (B) displaying a 500 × 700 nm^2 area of removed adsorbates. (F) A 300 × 300 nm^2 AFM image of the division between bare Au and dendrimer layer after shaving. (5) A cursor plot as indicated in (F) showing the height of dendrimers in relation to the bare Au. All STM imaging set points are 0.70 V and 20 pA.

TABLE 1: Ambient STM, UHV STM, and Solution Phase Measurements of the Long (a) and Short (b) Axes, Eccentricity (ε), STM Apparent Height (h_{APP}), Calculated Real Height (h_{REAL}), and Volume (V) on Characteristic Dendrimers

environment	*a* (nm)	*b* (nm)	ε	h_{APP} (nm)	h_{REAL} (nm)	V (nm^3)
ambient STM (Figure *1*)	6.0	5.3	0.47	0.59	2.8 ± 0.2	46.4 ± 5.0
ambient STM (av)	7.4 ± 0.9	6.1 ± 1.0	0.52 ± 0.25	0.46 ± 0.08	2.2 ± 0.2	44.6 ± 9.4
UHV STM (Figure *1*)	5.4	3.6	0.75	0.35	1.9 ± 0.2	18.1 ± 2.7
UHV STM (av)	4.6 ± 0.8	3.5 ± 0.8	0.60 ± 0.26	0.31 ± 0.07	1.8 ± 0.2	14.4 ± 4.0
solution[1]	4.5	4.5	0	n/a	4.5	47.7

region adjacent to the dendrimer's periphery, measures 0.59 nm. The averages of *a*, *b*, and h_{APP}, measured for over 100 dendrimers, are 7.4 ± 0.9, 6.1 ± 1.0, and 0.46 ± 0.08 nm, respectively. The ranges of *a* (5.7−9.3 nm), *b* (4.3−8.9 nm), and h_{APP} (0.20−0.68 nm) reveal the heterogeneity in dendrimer deformation upon immobilization. The fact that dendrimers deform on the surface under ambient conditions is consistent with previous investigation of dendrimers.[1,10,15]

To quantify and to compare the lateral deformation of individual surface-immobilized dendrimers the parameter of eccentricity, $\varepsilon = (1 - b^2/a^2)^{1/2}$, is utilized. For a perfect sphere, or circle, e.g., $d = 4.5$ nm, $\varepsilon = 0$, as $a = b = 4.5$ nm.[1] The values of *a* and *b*, measured from cursor plots 1 and 2 in Figure 1, yield $\varepsilon = 0.47$, quantify the noncircular nature at dendrimer contact. The range of ε determined from ambient STM imaging is 0−0.83 with an average of 0.52 ± 0.25. These nonzero values of ε quantify dendrimer deformation from their circular geometry at the interface.

Under UHV conditions, surface-bound dendrimers are also deformed and suffer significant volume loss. Figure 1C is a 100 × 100 nm^2 UHV STM topographical image of high coverage G4-PAMAM-OH-$(Pt^{2+})_{70}$ on Au(111). The sample shown in Figure 1C was prepared under identical conditions to the sample in Figure 1A. The first glance reveals that the individual dendrimers appear smaller in Figure 1C than those in Figure 1A, an indication of volume loss. Figure 1D is a 13 × 13 nm^2 high-resolution view of the surface in Figure 1C. Cursor profiles 3 and 4 correspond to the selected dendrimer in Figure 1D, from which *a*, *b*, and h_{APP}, are measured: 5.4, 3.6, and 0.35 nm, respectively, thus an ε of 0.75. In comparison to the G4 in Figure 1A, the dendrimers in Figure 1C deviate further from spherical shape and exhibit significantly smaller size. The selected dendrimer molecule in Figure 1D is typical of G4-PAMAM-OH-$(Pt^{2+})_{70}$ immobilized on Au(111) under UHV conditions. Over 100 dendrimers were measured under UHV conditions, displaying the dimensions of $a = 4.6 \pm 0.8$, $b = 3.5 \pm 0.8$, and $h_{APP} = 0.31 \pm 0.07$ nm. The ranges of *a* and *b* are wider under UHV, 2.9−6.8 nm and 1.9−5.8 nm, respectively, corresponding to ε range of 0−0.91 with an average $\varepsilon = 0.60 \pm 0.26$. The geometrical differences between ambient and UHV dendrimers, in terms of *a*, *b*, h_{APP}, and ε, suggest that the vacuum is responsible for further deformation and volume reduction of dendrimers.

The contrast in STM images depends on the physical height of dendrimers as well as the local density of states (LDOS) available for tunneling at specific imaging conditions.[32,36] We utilize AFM to calibrate the STM apparent height, taking advantage of genuine height measurements in AFM topographs.

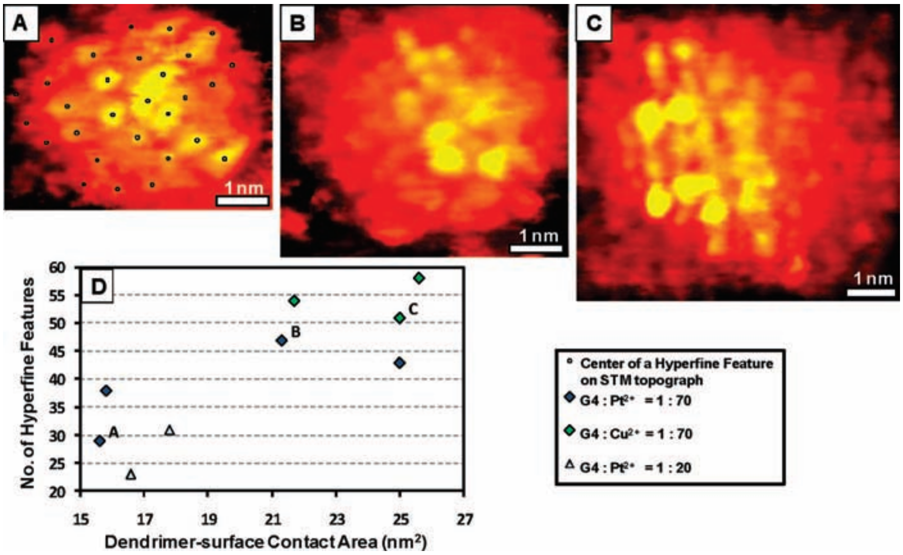

Figure 2. STM topographs reveal the hyperfine features and the trend that the number of observable hyperfine features increases with increasing dendrimer−Au surface contact area. (A) A high-resolution STM topograph of a G4 dendrimer treated with Pt(II). The 29 hyperfine features are indicated by small circles, and the surface contact area is 15.6 nm^2. (B) A high-resolution STM image revealing 47 hyperfine features for a G4 dendrimer treated with Pt(II) having an area of 21.3 nm^2. (C) A high-resolution STM image of a G4 dendrimer treated with Cu(II) and having 51 hyperfine features and an area of 25.0 nm^2. (D) This plot represents the trend of increased observation of hyperfine features with increased surface contact area. All STM imaging set points are ca. 0.70 V and 20 pA.

Figure 1E is a 1.8 × 1.8 μm^2 AFM topographical image of the same G4-PAMAM-OH-(Pt^{2+})$_{70}$ layer on Au(111) as Figure 1A, within which a 500 × 700 nm^2 area of adsorbates was displaced under a high force to expose the Au surface. Figure 1F is a zoom-in view (300 × 300 nm^2) at the edge of shaved area, in which the gold surface and individual dendrimers are clearly visible for height measurement. Cursor profile 5, as indicated in Figure 1F, shows the characteristic heights of the dendrimers, $h_{\mathrm{REAL}} = 2.8 \pm 0.2$ nm.

Because the lateral resolution of AFM is less than that of STM due to tip convolution,[16,37] the STM topographic images were used to extract the dimension and volume, upon AFM calibration of height. Following a similar approach reported previously,[36] a linear correlation is assumed between the STM apparent height and AFM height measured from the same sample: $h_{\mathrm{REAL}} = 3.13h_{\mathrm{APP}} + 0.83$. Table 1 summarizes the results for surface-bound dendrimers in UHV as well as in ambient media.

With the quantification of a, b, and h_{REAL}, the volume of each dendrimer may be calculated by assuming a elliptical cap geometry: $V_{\mathrm{CAP}} = (1/6\pi h_{\mathrm{REAL}})(3/4ab + h_{\mathrm{REAL}}^2)$.[38] Upon immobilization on the Au surface, the volume was measured to be 44.6 ± 9.4 nm^3 and was reduced to 14.4 ± 4.0 nm^3 in UHV. This volume decrease, from the solution phase 47.7 nm^3 ($V_{\mathrm{soln}} = (4/3)\pi r^3$) to the surface immobilized 44.6 nm^3, is consistent with prior observations by AFM.[7,39] In the case of G7-PAMAM-NH$_3$ dendrimers, the volume was reduced to 70% of its solution size after immobilization on mica surfaces.[39]

The loss of water molecules and resulting conformational changes are responsible for the observed deformations. In the spherical structure of PAMAM-OH dendrimers in aqueous phase, solvent H$_2$O molecules are present in the interior[7,39,40] forming hydrogen bonds with the electron negative moieties such as N or O atoms. Molecular dynamics simulations indicated that the interior of even G2-PAMAM dendrimers contains an overwhelming amount of H$_2$O to maintain their structural integrity.[40] The higher generations such as G4 and G5 are flexible without much strain at the termini and, therefore, intake more water molecules.[41] The slight reduction in volume (3.1 nm^3 or 6.5%) of immobilized dendrimers in ambient conditions is most likely due to the chemisorption of amines to Au surfaces,[13,15,42] leading to molecular deformation and expulsion of H$_2$O. The chemisorption energy of N−Au at room temperature is 4−7 kcal/mol,[42] and multiple anchors with gold surface are certainly sufficient to compete with H-bonds.[43] Due to the degassing in UHV conditions, the solvent molecules within dendrimers were likely removed, thus disrupting the H-bonds formed in ambient to maintain the conformational rigidity. As a result, the G4 in UHV only exhibits 30% of its original volume in solution.

Our approach takes the best advantage of AFM (height measurement) and STM (high lateral resolution and accuracy) to attain precise measurements of individual dendrimers' geometry, including a, b, and h. The advances discussed in this section with respect to prior structural characterizations are the finding of a noncircular interface and a more precise determination of geometrical parameters. The results from this investigation reveal precisely the deformations of dendrimers on surfaces, which provide new insights for applications involving surface-bound dendrimers such as devices[44−46] and catalysis.[5]

Capturing the Intramolecular Structures of Dendrimers. Figure 2A is a high-resolution STM topographical image of a G4-PAMAM-OH-(Pt^{2+})$_{70}$ dendrimer. Small protrusions in the STM topograph are visible at the exterior and are referred as "hyperfine features". The lateral dimensions of these hyperfine features range from 0.3 to 1.4 nm. These hyperfine features account for the surface roughness of individual dendrimers, whose values range from 0.03 to 0.10 nm in STM apparent height or 0.92 to 1.14 nm in true height. These hyperfine features were stable under the aforementioned STM imaging conditions. We underline that the highest resolution hyperfine features were captured only in ambient, an important fact in helping revealing imaging mechanism (discussed in the next section).

The center of each hyperfine feature is marked in Figure 2A to facilitate counting, and the total number for this dendrimer is 29 ± 1. The dendrimer−surface contact area, using ImageJ for accurate determination of the periphery, is 15.6 ± 0.2 nm^2. Figure 2B is another example of a high-resolution STM topographical image of a more deformed G4. In comparison with Figure 2A, the dendrimer in Figure 2B spreads more on the surface, contact area of 21.3 ± 0.2 nm^2, and exhibits 47 ± 1 hyperfine features. To verify the robustness of these observation, a dendrimer doped with Cu(II) ions was imaged as shown in Figure 2C. This G4-PAMAM-OH-$(Cu^{2+})_{70}$ shows 51 ± 3 hyperfine features under a dendrimer−surface contact of 25 ± 0.3 nm^2. Figure 2D displays a clear trend that the number of hyperfine features observed under STM increases with the increasing of dendrimer−surface contact, i.e., with the increasing of deformation upon immobilization on surfaces. Although there may be a dependence on metal character, e.g., the greater number of hyperfine features observed when doping G4 dendrimers with Cu^{2+} than with Pt^{2+}, the mechanism is unclear to us and remains a subject for future investigations.

These observed hyperfine features are consistent with the explanation that each feature represents the location of the −OH terminus. Collective evidence follows. First, hyperfine features are genuine intramolecular structural features of PAMAM-OH dendrimers because they were observed only within the confinement of the individual dendrimers. Second, hyperfine features are not STM contrast manifested from SAMs. In contrast to the SAM matrix, hyperfine features do not exhibit any long-range order. The interhyperfine feature separation ranges from 0.49 to 2.40 nm, which significantly differs from the 0.5 nm lattice constant of alkanethiol SAMs on Au(111). Third, the total number of observed hyperfine features never exceeds the number of termini. There are 64 hydroxyl groups in each G4-PAMAM-OH dendrimer. For simplicity we assume that these termini evenly distributed at the exterior of a G4 sphere in solution. Upon deformation on surfaces, the termini at the top region becomes more crowded but never exceeds 64. In our experiments, the number of hyperfine features observed ranges from 23 to 58, always less than 64 for G4, and does not exceed 128 for G5 dendrimers. Fourthly, the observed number of hyperfine structures increases with the increase of dendrimer-surface contact, and their separation is consistent with that estimated for termini in elliptic dome. The dendrimer displayed in Figure 2B exhibits representative geometry (a, b, h_{REAL} = 5.9 nm, 5.0 nm, 2.6 nm) with a 21.3 nm^2 contact and 47 visible hyperfine features. Assuming that dendrimers deform into an elliptical cap (or elliptical dome) shape with termini homogenously distributed at the outer surface, a simple geometry calculation $d_{CALC} = [(\pi h_{REAL}{}^2 + A_{SC})/N_{HF}]^{1/2}$ yields an average separation of 0.95 nm, where A_{SC} is the surface contact area between the dendrimer and substrate and N_{HF} is the number of hyperfine features counted for that dendrimer.[47] This estimation from simple geometry is in excellent agreement with the interhyperfine separation of 0.9 nm. Finally, the observation of hyperfine features are observed for Cu(II) saturated G4 as well as G5 dendrimers, as revealed in Figure 3. Hyperfine features of G4-PAMAM-OH are visible when doped with either Pt(II) (Figure 3A) or Cu(II) (Figure 3B). In addition, hyperfine features of higher generation dendrimer, G5-PAMAM-OH, are also visible upon doping with Pt(II) (Figure 3C) or Cu(II) (Figure 3D). Panels A−D of Figure 3 reveal 43, 54, 50, and 104 hyperfine features and areas of 21.7, 25.0, 19.2, and 48.6 nm^3, respectively. G4 and G5 STM topographs were recorded at similar imaging conditions: 1.0−0.7 V for G5 and 1.0−0.3 V for G4, both between 20 and 35 pA. The G5 dendrimers in Figure 3C and Figure 3D also agree well with the same trend: the number of observed hyperfine features increases with dendrimer−surface contact area. The observation of hyperfine features in our approach is of importance in dendrimer structural characterization because of its simplicity and resulting high resolution of 0.2 nm. This method should be applicable for dendrimers naturally containing conductive groups such as phenyl or metallic porphyrins and for those without conductive moieties as long as ligands are available for coordination with metal ions. The commonly encountered PAMAM and poly(propylimine) dendrimers have abundant amine and/or hydroxyl moieties, providing good coordination with metal(II) ions. Knowledge of intramolecular features is of great importance in many dendrimer applications such as drug delivery, for instance, in which designed drugs are carried by termini or interior functional groups.[2,44−46,48−50]

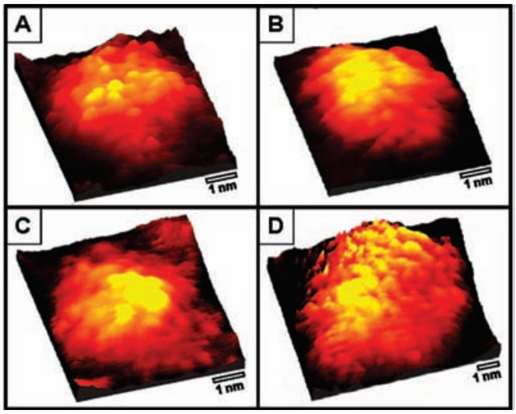

Figure 3. STM topographs of four types of dendrimers to reveal hyperfine features within: (A) G4-PAMAM-OH-$Pt(II)_{70}$ (V_b = 0.7 V, I_t = 20 pA); (B) G4-PAMAM-OH-$Cu(II)_{70}$ (V_b = 1.0 V, I_t = 20 pA); (C) G5-PAMAM-OH-$Pt(II)_{140}$ (V_b = 1.0 V, I_t = 20 pA); (D) G5-PAMAM-OH-$Cu(II)_{140}$ (V_b = 1.0 V, I_t = 25 pA).

STM Imaging Mechanism. In UHV, the STM-G4 imaging mechanism is consistent with metal nanoparticles encapsulated by dendrimers. Figure 4A displays a typical $I-V$ spectrum acquired atop a selected dendrimer. Under the initial condition of 1.0 V and 25 pA, the Coulomb blockade (CB) measured from the spectrum is 1.1 V. The $I-V$ spectrum shown in Figure 4B is typical for G4-PAMAM-OH-Pt_{70} dendrimers. From over 100 dendrimers measured under UHV, the average CB is 1.0 ± 0.3 eV. This observation of single electron tunneling (SET) behavior is similar to that of 1.4 nm Au nanoparticles covered by n-octanethiol and octanedithiol, as shown in the dashed curve.[26] This comparison suggests that the Pt(II) ions are most likely reduced to form Pt(0) nanoparticles by the STM tunneling electrons under UHV. If there were 70 Pt(II) ions and all were reduced, one would expect the particle size to be 1.26 nm. The size of the metal nanoparticles may be estimated from the $I-V$ spectrum:[51,26] The total capacitance at the tunneling junction is calculated from $C_t = e/\mathrm{CB}$ = 0.15 aF. The diameter of the Pt nanoparticles, d_{NP}, is then estimated using $d_{NP} = C_t/(2\pi\varepsilon_d\varepsilon_0)$, where ε_d is the dielectric constant of dendrimer surrounding the NP and ε_0 is the permittivity of the vacuum. With the C_t = 0.15 aF, and $\varepsilon_d = 2.3$ using the thiol SAM as an approximation of the dendrimer dielectric constant,[26] and $\varepsilon_0 = 8.854 \times 10^{12}$ F/m for vacuum, [52] the d_{NP} is 1.1 nm. This diameter is equivalent to a nanocrystal containing 51 Pt(0) atoms; thus not all Pt(II) ions were reduced or not all sites bound to Pt(II). The $I-V$ spectra for prereduced dendrimers did not show SET behavior.[22] This was attributed to the higher degree of structural changes or deformation for these dendrimers containing metal NPs in UHV.[22] To avoid dendrimer structural change before metal ion reduction, we used G4 and G5 with metal(II) directly and without prereduction. The in situ and transient reduction by tunneling electrons in UHV allows SET behavior to be revealed.

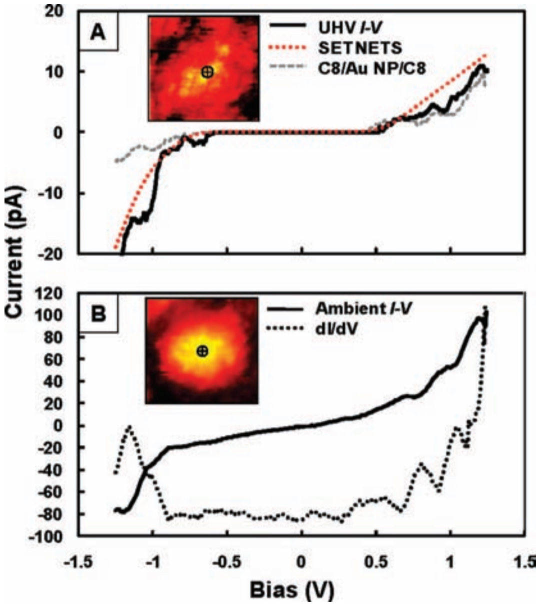

Figure 4. Scanning tunneling spectroscopy of metal-treated G4 dendrimers displaying SET characteristics. (A) An *I*−*V* curve taken under UHV conditions (set point: 1.00 V, 25 pA). The gray (dashed) *I*−*V* curve from a previous NP publication[26] and the red dot DBTJ fit curve are shown for comparison. (B) An *I*−*V* curve taken atop the dendrimer in the insert (the point of spectroscopy is noted) under ambient conditions (set point: 0.71 V, 13 pA). The associated relative d*I*/d*V* (dashed) curve is shown to clarify the current increase at the CS steps.

Following the common practice in SET investigation, a double barrier tunnel junction (DBTJ) model[26,51,53] is used to attain the equivalent circuit. The result of our nonlinear fitting using SETNETS freeware is revealed in Figure 4A (red curve). The fitting agrees well with the *I*−*V* spectrum in the negative bias and CB regions and exhibits a slight deviation in the positive bias above CB. Our resulting circuit parameters are R_1 (0.09 GΩ) and C_1 (0.12 aF) of the NP/Au electrode junction and R_2 (0.38 GΩ) and C_2 (0.05 aF) for the NP/STM tip junction, with a fractional residual charge of $0.08e^-$. For comparison, Figure 4A also shows the results from a ethanedithiol/ethanethiol-encapsulated Au NP.[26] The similarity is very evident.

Under ambient conditions, the *I*−*V* spectrum differs from that in UHV. Figure 4B displays a *I*−*V* spectrum obtained atop a selected G4 dendrimer in air. First, there is no observable CB. In addition, the overall slope differs from the *I*−*V* spectrum acquired for G5-PAMAM dendrimers containing prereduced Au NPs (d_{AuNP} = 1.7 nm),[22] where the presence of Coulumb staircases (CS) was evident and with much higher conductivity than our G4-PAMAM-OH-$\mathrm{Pt}^{2+}{}_{70}$.[22] Furthermore, the *I*−*V* spectra of alkanethiol covered Au-NPs exhibit SET behavior.[26,54,55] Finally, other dendrimers contain conductive functionalities such as Ru ions,[25] or phenyl rings,[24] exhibit similar conductivity, and permit high-resolution STM imaging in ambient conditions.[38] Taken collectively, we infer that the incorporation of metal ions alters the LDOS of G4 and increases the tunneling probability from unmodified dendrimers, thus enabling the high-resolution imaging of intramolecular features. The rich LDOS structure is also reflected in the peaks in the d*I*/d*V* plot under the *I*−*V* spectrum in Figure 4B. Figure 5 compares and illustrates the two scenarios schematically; i.e., Pt(0) NP formed by tunneling electron reduction of Pt(II) ions is encapsulated by G4 under UHV and Pt(II) ions remain coordinated to tertiary amines within G4 under ambient conditions.

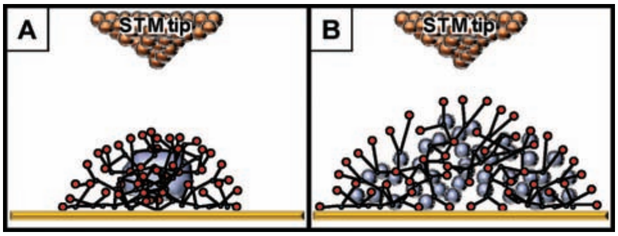

Figure 5. A schematic diagram of STM imaging and *I*−*V* spectroscopy on G4 dendrimers immobilized on Au(111) suggest (A) Pt(0) NP formation under UHV conditions and (B) a lowering of the tunneling barrier with Pt(II). Both pathways alter the LDOS of dendrimers allowing for hyperfine feature resolution.

Conclusions

This work introduces a simple method of applying high-resolution STM imaging to insulators such as fourth and fifth generations of poly(amidoamine) hydroxyl-terminated dendrimers. Our approach of lowering the tunneling barrier takes advantage of the ligand functionalities within the molecules, such as tertiary amines, which can coordinate with Pt^{2+} or Cu^{2+}. This pretreatment is proven to be effective as evidenced by the ultrahigh resolution of intramolecular hyperfine features. The spatial distribution, size, and overall number of hyperfine features are consistent with the location of dendrimer termini. The number of observable hyperfine features also increases with the higher degree of deformation on surfaces. Combining STM and AFM, the fundamental parameters of individual dendrimers, including axis, height, asphericity, and volume, are determined with high precision. From STM spectroscopy and previous work of STM imaging of dendritic systems, the STM imaging mechanism under ultrahigh vacuum is consistent with metal nanoparticles encapsulated by dendrimers, while ambient imaging is most likely via metal-ions-facilitated charge transport. Work is in progress to apply similar approaches to (a) higher generations of dendrimers, (b) dendrimers upon tagging of specific moieties via metal ions, (c) other insulator systems such as polymers and composite materials, and (d) proteins. We also hope this investigation would attract more theoretical work to understand the dendrimer conformation and detailed STM imaging mechanism. The visualization of hyperfine structures is of importance in many dendrimer-based applications such as (a) drug delivery in which designed molecules are carried by termini or intramolecular functionalities and (b) devices in which dendrimers are immobilized on circuit boards. This ultrahigh resolution brings us closer to atomistic characterization of dendrimer confirmations and should also enable direct comparison of dendrimer structures with simulations and, therefore, deepen our understanding of charge transport in dendrimer systems, as well as intramolecular and molecule−surface interactions.

Acknowledgment. We thank Professor Richard Crooks at The University of Texas at Austin for his insightful information with respect to dendrimer preparation and metal coordination. We also thank Dr. Thomas J. Mullen, Mr. Yih Horng Tan, and Mr. Shawn Reichers at UC Davis for many helpful discussions. We also acknowledge Dr. Guohua Yang at Creatv Microtech, Inc., and Professor Li Tan at The University of Nebraska, Lincoln, for their initial experimental effort toward this project when they were at UC Davis. We would also like to thank Professor Peter Hadley at Graz University of Technology, Austria, for use of the SETNETS program. Y. Liu is a recipient of the CPIMA SURE program for undergraduate students. We appreciate the financial support from the University of California, Davis, and an NSF-MRSEC grant through Stanford University's CPIMA Program.

References and Notes

(1) Scott, R. W. J.; Wilson, O. M.; Crooks, R. M. *J. Phys. Chem. B* **2005**, *109*, 692.

(2) Patri, A. K.; Majoros, I. J.; Baker, J. R. *Curr. Opin. Chem. Biol.* **2002**, *6*, 466.

(3) Xie, H.; Gu, Y. L.; Ploehn, H. J. *Nanotechnology* **2005**, *16*, S492.

(4) Lee, C. C.; MacKay, J. A.; Frechet, J. M. J.; Szoka, F. C. *Nat. Biotechnol.* **2005**, *23*, 1517.

(5) Niu, Y. H.; Crooks, R. M. *C. R. Chim.* **2003**, *6*, 1049.

(6) He, J. A.; Valluzzi, R.; Yang, K.; Dolukhanyan, T.; Sung, C. M.; Kumar, J.; Tripathy, S. K.; Samuelson, L.; Balogh, L.; Tomalia, D. A. *Chem. Mater.* **1999**, *11*, 3268.

(7) Muller, T.; Yablon, D. G.; Karchner, R.; Knapp, D.; Kleinman, M. H.; Fang, H. B.; Durning, C. J.; Tomalia, D. A.; Turro, N. J.; Flynn, G. W. *Langmuir* **2002**, *18*, 7452.

(8) Li, J.; Qin, D. J.; Baker, J. R.; Tomalia, D. A. *Macromol. Symp.* **2001**, *167*, 257.

(9) Chen, A. M.; Santhakumaran, L. M.; Nair, S. K.; Amenta, P. S.; Thomas, T.; He, H. X.; Thomas, T. J. *Nanotechnology* **2006**, *17*, 5449.

(10) Gu, Y.; Xie, H.; Gao, J.; Liu, D.; Williams, C. T.; Murphy, C. J.; Ploehn, H. J. *Langmuir* **2005**, *21*, 3122.

(11) Abdelhady, H. G.; Allen, S.; Davies, M. C.; Roberts, C. J.; Tendler, S. J. B.; Williams, P. M. *Surf. Sci.* **2004**, *558*, 99.

(12) Hierlemann, A.; Campbell, J. K.; Baker, L. A.; Crooks, R. M.; Ricco, A. J. *J. Am. Chem. Soc.* **1998**, *120*, 5323.

(13) Lackowski, W. M.; Campbell, J. K.; Edwards, G.; Chechik, V.; Crooks, R. M. *Langmuir* **1999**, *15*, 7632.

(14) Li, J.; Piehler, L. T.; Qin, D.; Baker, J. R.; Tomalia, D. A.; Meier, D. J. *Langmuir* **2000**, *16*, 5613.

(15) Hiraiwa, D.; Yoshimura, T.; Esumi, K. *J. Colloid Interface Sci.* **2006**, *298*, 982.

(16) Allen, M. J.; Hud, N. V.; Balooch, M.; Tench, R. J.; Siekhaus, W. J.; Balhorn, R. *Ultramicroscopy* **1992**, *42*, 1095.

(17) Senden, T. J. *Curr. Opin. Colloid Interface Sci.* **2001**, *6*, 95.

(18) Eigler, D. M.; Schweizer, E. K. *Nature* **1990**, *344*, 524.

(19) Eigler, D. M.; Weiss, P. S.; Schweizer, E. K.; Lang, N. D. *Phys. Rev. Lett.* **1991**, *66*, 1189.

(20) Stroscio, J. A.; Eigler, D. M. *Science* **1991**, *254*, 1319.

(21) Merz, L.; Hitz, J.; Hubler, U.; Weyermann, P.; Diederich, F.; Murer, P.; Seebach, D.; Widmer, I.; Stohr, M.; Guntherodt, H. J.; Hermann, B. A. *Single Mol.* **2002**, *3*, 295.

(22) Nijhuis, C. A.; Oncel, N.; Huskens, J.; Zandvliet, H. J. W.; Ravoo, B. J.; Poelsema, B.; Reinhoudt, D. N. *Small* **2006**, *2*, 1422.

(23) Gillies, E. R.; Frechet, J. M. J. *Drug Discovery Today* **2005**, *10*, 35.

(24) Li, W. S.; Kim, K. S.; Jiang, D. L.; Tanaka, H.; Kawai, T.; Kwon, J. H.; Kim, D.; Aida, T. *J. Am. Chem. Soc.* **2006**, *128*, 10527.

(25) Latterini, L.; Pourtois, G.; Moucheron, C.; Lazzaroni, R.; Bredas, J. L.; Kirsch-De Mesmaeker, A.; De Schryver, F. C. *Chem.—Eur. J.* **2000**, *6*, 1331.

(26) Yang, G. H.; Tan, L.; Yang, Y. Y.; Chen, S. W.; Liu, G. Y. *Surf. Sci.* **2005**, *589*, 129.

(27) Riposan, A.; Li, Y.; Tan, Y. H.; Galli, G.; Liu, G. Y. *J. Phys. Chem. A* **2007**, *111*, 12727.

(28) Pellechia, P. J.; Gao, J. X.; Gu, Y. L.; Ploehn, H. J.; Murphy, C. J. *Inorg. Chem.* **2004**, *43*, 1421.

(29) Zhao, M. Q.; Sun, L.; Crooks, R. M. *J. Am. Chem. Soc.* **1998**, *120*, 4877.

(30) Yang, G. H.; Liu, G. Y. *J. Phys. Chem. B* **2003**, *107*, 8746.

(31) Kang, J. F.; Ulman, A.; Liao, S.; Jordan, R.; Yang, G. H.; Liu, G. Y. *Langmuir* **2001**, *17*, 95.

(32) Riposan, A.; Liu, G. Y. *J. Phys. Chem. B* **2006**, *110*, 23926.

(33) Yang, G. H.; Qian, Y. L.; Engtrakul, C.; Sita, L. R.; Liu, G. Y. *J. Phys. Chem. B* **2000**, *104*, 9059.

(34) Liu, G. Y.; Xu, S.; Qian, Y. L. *Acc. Chem. Res.* **2000**, *33*, 457.

(35) Hutter, J. L.; Bechhoefer, J. *Rev. Sci. Instrum.* **1993**, *64*, 1868.

(36) Bumm, L. A.; Arnold, J. J.; Dunbar, T. D.; Allara, D. L.; Weiss, P. S. *J. Phys. Chem. B* **1999**, *103*, 8122.

(37) VanCleef, M.; Holt, S. A.; Watson, G. S.; Myhra, S. *J. Microsc. (Oxford, U.K.)* **1996**, *181*, 2.

(38) Diaz, D. J.; Storrier, G. D.; Bernhard, S.; Takada, K.; Abruna, H. D. *Langmuir* **1999**, *15*, 7351.

(39) Mecke, A.; Lee, I.; Baker, J. R.; Holl, M. M. B.; Orr, B. G. *Eur. Phys. J. E* **2004**, *14*, 7.

(40) Lee, I.; Athey, B. D.; Wetzel, A. W.; Meixner, W.; Baker, J. R. *Macromolecules* **2002**, *35*, 4510.

(41) Maiti, P. K.; Cagin, T.; Wang, G. F.; Goddard, W. A. *Macromolecules* **2004**, *37*, 6236.

(42) Hoft, R. C.; Ford, M. J.; McDonagh, A. M.; Cortie, M. B. *J. Phys. Chem. C* **2007**, *111*, 13886.

(43) Markovitch, O.; Agmon, N. *J. Phys. Chem. A* **2007**, *111*, 2253.

(44) Hong, S. P.; Bielinska, A. U.; Mecke, A.; Keszler, B.; Beals, J. L.; Shi, X. Y.; Balogh, L.; Orr, B. G.; Baker, J. R.; Holl, M. M. B. *Bioconjugate Chem.* **2004**, *15*, 774.

(45) Liu, M.; Fréchet, J. M. J. *Pharm. Sci. Technol. Today* **1999**, *2*, 393.

(46) Malik, N.; Evagorou, E. G.; Duncan, R. *Anti-Cancer Drugs* **1999**, *10*, 767.

(47) Harris, J. W. S., H. *Handbook of Mathematics and Computational Science*; Springer-Verlag: New York, 1998.

(48) Esfand, R.; Tomalia, D. A. *Drug Discovery Today* **2001**, *6*, 427.

(49) Haensler, J.; Szoka, F. C. *Bioconjugate Chem.* **1993**, *4*, 372.

(50) Quintana, A.; Raczka, E.; Piehler, L.; Lee, I.; Myc, A.; Majoros, I.; Patri, A. K.; Thomas, T.; Mule, J.; Baker, J. R. *Pharm. Res.* **2002**, *19*, 1310.

(51) Fan, F. R. F.; Bard, A. J. *Science* **1997**, *277*, 1791.

(52) *CRC Handbook of Chemistry and Physics*, 88th ed.; CRC Press/Taylor & Francis: Boca Raton, FL, 2008.

(53) Tinkham, A. E. H. a. M. *Phys. Rev. B* **1991**, *44*, 5919.

(54) Andres, R. P.; Bein, T.; Dorogi, M.; Feng, S.; Henderson, J. I.; Kubiak, C. P.; Mahoney, W.; Osifchin, R. G.; Reifenberger, R. *Science* **1996**, *272*, 1323.

(55) Fuchs, D. J. Probing Nanoparticle Assemblies and Substrate Effects on Self-Assembled Monolayers. Doctoral Dissertation, Pennsylvania State University, 2004.

JP810535G